UTRECHT UNIVERSITY. MPOC

Turbulence related quantities in the surface layer of Lake Garda.

Francesco Cassano

July 12, 2017

Abstract

The purpose of this study is the investigation of turbulence related quantities in Lake Garda. The research is based on in-situ observations of the vertical shear and temperature micro-structure in the surface layer, using a vertical microstructure profiler (microCTD). The aim is to quantify the dissipation of energy due to turbulent motion under the assumption of locally isotropic and homogeneous turbulence, and to identify and describe the main sources of turbulent mixing. The Nasmyth spectrum method is used to compute the dissipation of Turbulent Kinetic Energy (TKE) rate, while the mixing coefficient is computed using the Osborn theory. The analysis is carried out for the months of March, April and May and focuses on the northern, narrow part of the lake: here, the Earth's rotation forces a secondary closed circulation characterized by strong vertical transport at the sides of the basin. The observations, supported by the atmospheric forcing analysis, are used to infer the role of turbulent mixing in the phytoplankton growth and productivity. The result reveals a large unevenness in the horizontal distribution of phytoplankton in early Spring: in the eastern part of the lake the Chlorophyll is completely depleted by the upwelling of cold deep water, while on the other side of the basin, significant amounts Chlorophyll are found at extreme depths due to the Ekman downwelling.

Contents

1 Introduction

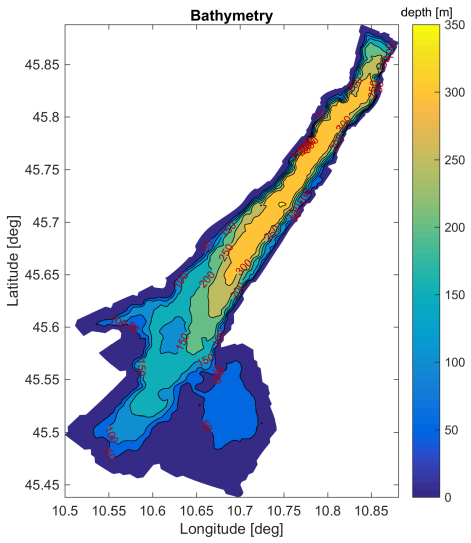

Figure 1.1: The bathymetry of Lake Garda.

Lake Garda is the largest lake in Italy. It is located in the north of the country between Trento, Brescia, Verona (46.6° N - 10.6° E), 65 m over the sea level. It develops in the North-South direction delimited laterally by steep sides; its bottom is almost flat with the exception of the Sirmione area, where the depth rapidly varies from 50 to 100 meters; the maximum depth and surface measure 346 m and 368 m^2 respectively. Its main inflow (Sarca river) is located at the northern edge.

The limnological investigations carried out during in the past years showed Lake Garda conditions range from oligotrophy to mesotrophy [Salmaso, 2005]. This trophic classification identifies lakes with low algae productivity and relatively clear water; the bottom waters are generally well oxygenated and present a medium level of (algae) nutrients.

The vertical structure of the Lake Garda can be described in terms of its temperature profile and it is strongly affected by the seasonal cycle. Garda is an oligomictic lake, which is usually thermally stable but occasionally undergoes a complete overturn. This strong mixing event allows the well oxygenated surface waters to mix with the nutrient rich waters from the bottom boundary layer.

In a recent work [M. Toffolon 2012], the effect of Earth's rotation on the wind driven circulation in narrow alpine lakes is investigated. The layer where the Coriolis force is balanced by the momentum flux is called surface Ekman layer: here, the horizontal velocity of the flow is a function of depth, and its direction changes along the vertical describing the so-called Ekman spiral. By tanking into account the lateral transfer of momentum due to the horizontal eddy viscosity, Toffolon proposed both analytic and numerical solutions of the flow in the vertical cross-section, without the necessity of introducing lateral boundary layers. His results showed that when a steady wind blows along the lake's main axis, a closed secondary circulation is induced in the plane orthogonal to the wind direction, resulting in strong vertical transport at the lake's sides: with respect to the wind direction, upwelling on the left side and downwelling on the right side. The lateral variations

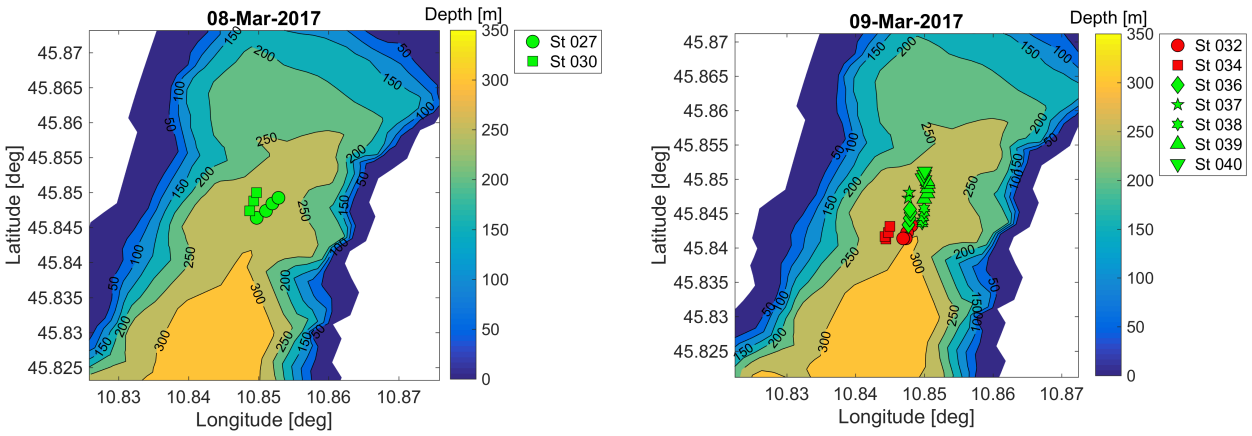

Figure 2.1: The bathymetry and coordinates of the first two days of measurements. As both maps show, during these days we focused on sampling the APPA site.

of vertical velocity are found to be highly dependent on the anisotropy parameter α:

$$\alpha = \frac{D_0}{W}\sqrt{\frac{\nu_H}{\nu_V}} \tag{1.1}$$

Where D_0 is the depth, W is the transverse length of the basin, ν_H, ν_V are the horizontal and vertical eddy viscosity. Thus, the anisotropy parameter α represents the differential spreading of turbulent momentum. An analysis of the Ekman secondary circulation is carried out for Lake Garda, using in-situ observations of the turbulent mixing processes of water column. The main focus is to determine its effect on the vertical structure of the surface layer and the impact of the strong vertical mixing on the phytoplankton population. In section 2 an overview of the data-set, the survey procedure, research site and methods is given. In section 3 the results are presented along with the meteorological forcing analysis. The investigation focuses on: the quantification of the surface buoyancy heat flux and wind stress [section 3.1]; the analysis of the spatial variability of the surface layer turbulent mixing [section 3.4]; the evolution of the surface layer features over 3 months (March, April and May) [section 3.2]; the investigation of the effect of Ekman circulation on the phytoplankton vertical distribution [section 3.3] .

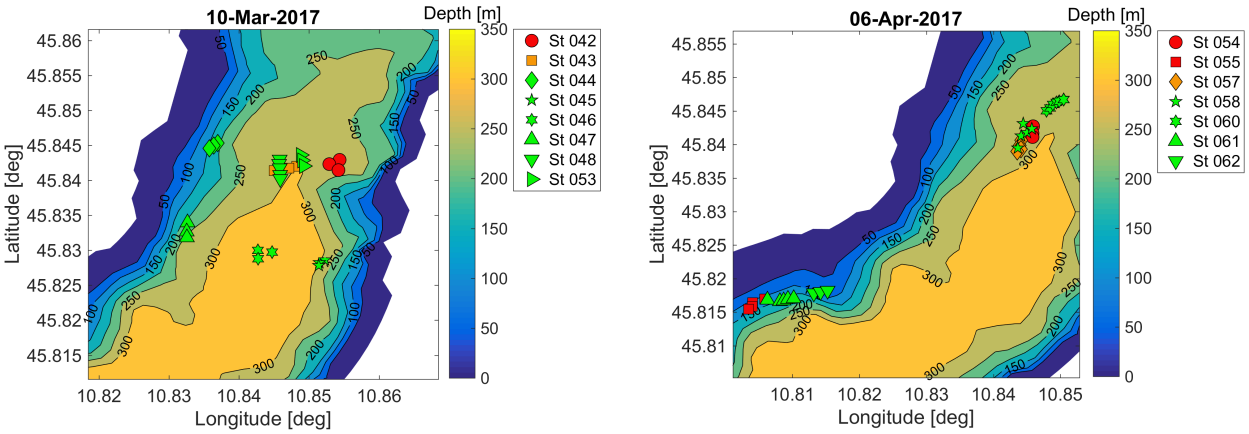

Figure 2.2: The bathymetry and coordinates of the third and fourth days of measurements. On the third day (left) in addition to the APPA site, we sampled the lake along two longitudinal transects. On the fourth day (right) several water profiles were measured offshore of Limone.

2 Data and methods

2.1 Data and instrumentation

The main tool of our research is a vertical microstructure profiler (VMP - MicroCTD, manufactured by Rockland Scientific International). The main probe measures conductivity, temperature and pressure at a sampling frequency of 64 Hz. The microCTD is also equipped with 6 fast response sensors consisting in: 2 thermistors, used to determine the vertical micro-structure of temperature and temperature gradient, 2 shear probes, whose data is used to compute the dissipation of Turbulent Kinetic Energy (TKE), chlorophyll and turbidity sensors to study the mixing process and biological activity of the lake; all the fast probes sample at 512 Hz. The maximum depth reachable by the VMP is 100 m. The Chl *a* is found in the pigments of every photosynthesizing organism, such as algae, plants and phytoplankton and its concentration is quantified by the fluorimeter measurements. The radiative energy absorbed by the molecule of Chl *a* for the photosynthesis is then remitted as fluorescence radiation or as heat in the non-photochemical quencing. The Chl *a* concentrations detected with the fluorimeter are a proxy for the photosynthesis productivity, which in turn is regulated by the presence of nutrients, by the solar radiation intensity and by the water temperature.

The metereological data-set used in the analysis consists in: wind speed and direction, air temperature, relative humidity and shortwave radiation. Short wave radiation by the meteorological on-land station of Torbole[1], wind speed and direction were measured in Torbole and in Limone[2], the others were sampled on-board at approximately 2 m from the surface using the thermo-hygrometer. The data was sampled with different time steps: temperature relative humidity and shortwave radiation every 15 min, wind speed every 10 min while the wind direction every 10 min in Torbole and hourly in Limone. The surface temperature data is not periodically sampled, hence the rest of the meteorological variables have been interpolated in correspondence of surface temperature data.

Figure 2.3: The micro CTD.

Probes		Range	Accuracy	Resolution
Shear		[0,10] s^{-1}	5%	10^{-3} $s^{-}1$
Micro-Temp FP07		[-5,35] °C	0.005 °C	10−5 °C
Pressure		[50,100] bar	0.1% FS	5×10^{-4} bar
Vibration		[-1,1] g	2%	3×10^{-5} g
JAC	Temperature	[3,45] °C	0.01 °C	0.001 °C
	Conductivity	[2,65] mS cm^{-1}	0.01 mS cm^{-1}	0.001 mS cm^{-1}
Fluorescence		[0,400] ppb	0.1% FS	0.01 ppb
Turbidity		[0,1000] FTU	0.3 FTU	0.03 FTU

Table 2.1: The sensors specifications of the microCTD vertical microprofiler

2.2 The sampled sites

The measurements were gathered in different sites, all located in the northern part of the lake. The microCTD was always cast between 0 and the 100 m of depth, at each station several consecutive profiles were sampled as shown in fig.2.1-2.2-2.4-2.5. In order to investigate the spatial variability of the turbulence related quantities, two different areas of the lake were sampled: the APPA and Limone sites. Both these regions are located in the northern part of the lake, hence one would expect to find similar vertical structure and phytoplankton activity. Instead, they show very different features. These differences are mainly caused by different exposure to the meteorological forcing,

[1]http://www.meteotrentino.it
[2]http://www.arpalombardia.it

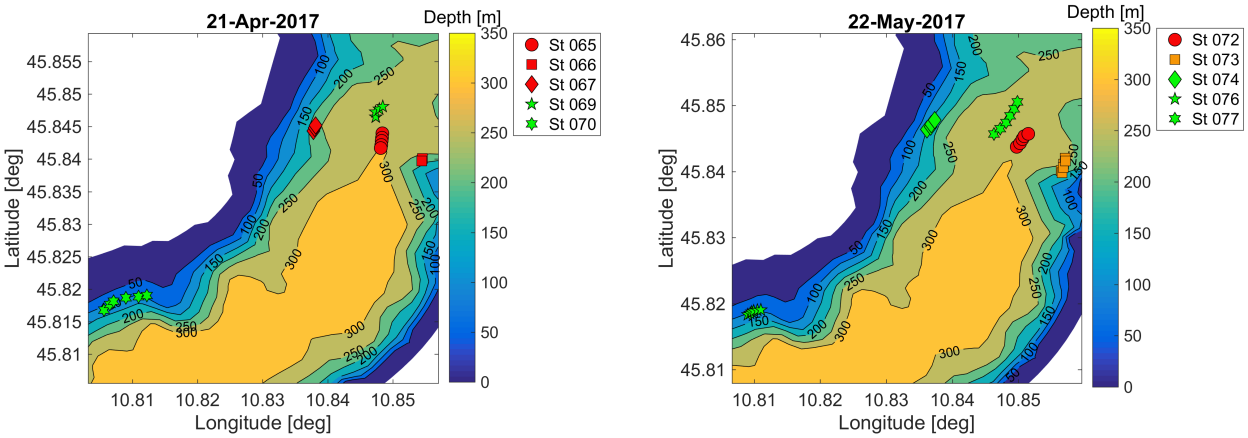

Figure 2.4: The bathymetry and coordinates of the fifth and sixth days of measurements. On both occasions the APPA site along with Limone and the transect were sampled.

one being located at the center of the basin and well exposed to the wind, the other being close to the western coast and therefore sheltered from the wind.

APPA[3] is the provincial agency for environmental protection, which regularly monitors Lake Garda at the coordinates: 45.85 N - 10.85 E (APPA site). Most of the observations were made here, where the maximum depth is 300 m. With the APPA data set, an analysis of the inter seasonal variation of turbulent mixing and its effect on the phytoplankton activity is carried out and supported by the atmopheric forcing analysis.

Several other profiles were measured in Limone (coordinates: 45.81 N - 10.81 E. Depth: 150 m), which is about 6 km south-west of the APPA point. Typically Limone's surface layer is warmer and more stable than APPA's. A comparison between the two data sets (APPA vs Limone) is carried out to have insights on the spatial variability of Lake Garda turbulence. The average length of the transect is $W \sim 1500$ m.

Additional longitudinal transects (left plot in fig.2.2 a in fig.2.4) centered on the APPA site were sampled. This survey aims at proving the existence of the Ekman transport at the sides of Lake Garda.

[3]Agenzia Provinciale per la Protezione dell'Ambiente

2.3 Methods

Pre-processing The microCTD was deployed multiple times in the same location and it continuously sampled the water column during both the downcast and the upcast. During the downcast the microCTD sinks at an almost constant speed of ~0.75 m/s. As the downcast is more representative of the unperturbed water column, the data was trimmed to separate different profiles within the same station. In order to smooth the signal, low-pass and band-pass filter were applied to the data: the cut-off frequency varies depending on the sampling frequency and the variable. Binning the profile was necessary in order to estimate the dissipation of TKE.

Estimation of TKE dissipation ε In 1941, Kolmogorov derived the spectrum of turbulent velocity fluctuations assuming the energy containing scale is much larger than the dissipative, also known as the Kolmogorov scale η. He predicted that within this range, the turbulent velocity fluctuation spectrum would follow the power law $\phi(k) \sim k^{-5/3}$, where ϕ is the spectrum and k the wave number. On these assumption the power spectral density of the turbulent velocity shear fluctuations will be proportional to $\sim k^{-1/3}$ [Kolmogorov, 1941]. Oakey derived an empirical shear velocity spectrum for scales comparable to the Kolmogorov's, based on a previous work of Nasmyth [Oakey, 1982]. From here on, we will refer to the empirical shear velocity spectrum as Nasmyth spectrum. The rate of dissipation of TKE can be evaluated as:

$$\varepsilon = \frac{15}{2}\nu\overline{\left(\frac{\partial u}{\partial z}\right)^2} = \int_0^\infty \phi(k)\,dk \tag{2.1}$$

Where ν is the kinematic viscosity and ϕ the shear spectrum. The computation of ε requires the estimation of the integral in eq.2.1 at wave number close to $k \sim 1/\eta$, where the measurements are strongly affected by the instrument noise. To reduce the effect of noise on the ε estimation, the Nasmyth spectrum is fitted to the observed shear spectrum and integrated on a finite range $[0, K_{MAX}]$. The spectral minimum is used to set the value of K_{MAX}. An example of the Nasmyth spectrum method is shown in fig.2.6: the cumulative distribution of the spectrum shows that 50% of the total area is found before the spectral maximum around $k \sim 15$ cpm; the effect of the noise is already appreciable at $k \sim 30$ cpm and its effect increase with the wave number k. The upper limit of the integration is set close to spectral minimum, so that the total integral of the Nasmyth spectrum represents the 93% of the measured one. This procedure reduces the overestimation of ε due to the instrument noise.

This method is applied to different segments along the vertical profile. The vertical profile of velocity shear is divided in overlapping segments of 2133 observations, the overlap consists in 196

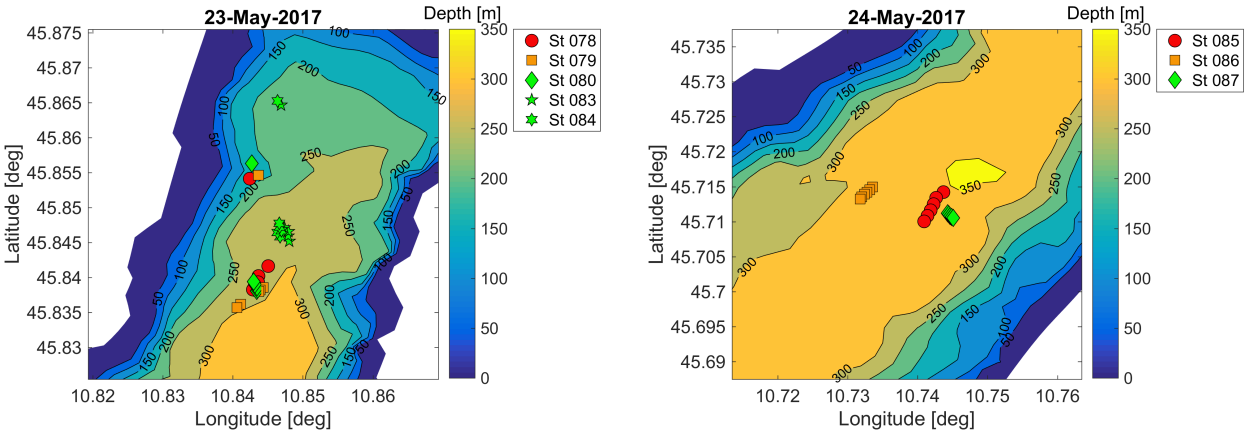

Figure 2.5: The bathymetry and coordinates of the seventh and eighth days of measurements. On the 23 of May the survey focused on the APPA site only, on the 24th of May the deepest part of the lake was sampled.

samples. In each segment 4 spectral estimates of dissipation ε are computed and averaged. The result is a vertical profile of ε binned every 2.5 m on average.

Unit	bin size	diss_length	overlap	fft_length
meters*	2.50	3.125	0.625	0.5
seconds	3.34	4.167	0.834	1.04
samples	1710	2133	196	532

Table 2.2: The bin is based on the number of samples, hence we estimated an average bin length in meters

Brunt-Vaisala Frequency, Thermal eddy diffusivity and Well Mixed Layer Depth The Brunt Vaisala frequency squared N^2 was computed in each bin as the best linear fit of the background density ($\delta\overline{\rho}/\delta z$) times $g/\overline{\rho}$. The turbulent mixing coefficient was derived from ε, considering that part of the turbulent kinetic energy enables the diffusion process instead of being dissipated by the viscous forces [Osborn 1980]. The thermal eddy diffusivity K_T was determined using the Osborn relation $K_T = \Gamma\varepsilon/N^2$, thus the patterns of thermal eddy diffusivity resemble those of the TKE dissipation.[4]

The well mixed layer depth was identified as: the bottom boundary of the surface layer containing the same amount of heat as the entire water column [Austin and Allen 2011]. If δz_i is the bin size, T_i the temperature of the i-th bin, T_B the deepest sampled temperature and T_S the surface

[4]See Appendix for the detailed derivation

temperature, the WML depth Z_{WML} is found according to the following formula:

$$Z_{\mathrm{WML}} = \sum_{i=1}^{N} \frac{(\mathrm{T}_S - \mathrm{T}_i) \cdot \delta z_i}{\mathrm{T}_S - \mathrm{T}_B} \tag{2.2}$$

We found this method to be less computational demanding than other segments-based algorithms [Abdulla et al., 2016], and at the same time more accurate than threshold-based methods, yet it resulted unreliable when applied to an almost homogeneous water column.

Surface fluxes The meteorological data described in section 2.1 were used to compute the surface wind stress τ, the total heat flux Q_o, the buoyancy flux B_o and the Monin-Obukov length L_{MO}.

The net surface heat flux Q_o represents the amount of heat exchanged between the atmosphere and the lake per square meter and per second and it is given by the sum:

$$Q_{\mathrm{o}} = Q_{\mathrm{sw}} + Q_{\mathrm{lw}} + Q_{\mathrm{e}} + Q_{\mathrm{h}}$$

Where the different components are respectively: net short wave radiation Q_{sw}, net longwave radiation Q_{lw}, latent heat flux Q_{e}, and the sensible heat flux Q_{h}. The net surface heat flux and its component were computed using the Lake Heat Flux Analyzer (LHFA) [Woolway et al., 2015].

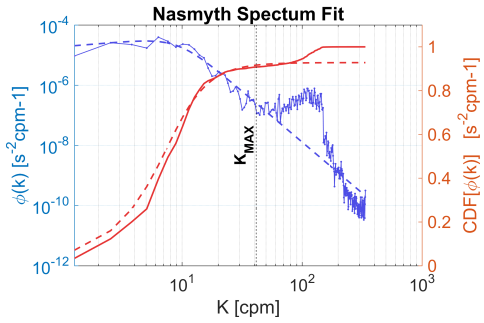

Figure 2.6: Example of Nasmyth spectrum fit: on the right axis (blue) are plotted the measured spectrum (solid) and the Nasmyth spectrum (dashed), on the right axis (red) are plotted the cumulative distribution of both spectra, each normalized over the area beneath the observed spectrum. The vertical black dashed line indicates the upper limit of integration of the Nasmyth spectrum.

The wind stress τ quantifies the amount of momentum transferred from the wind to the lake, per squared meter and per second. This momentum flux was computed as $\tau = \rho_{\mathrm{air}} \mathrm{C}_D \mathrm{U}^2$, where $\rho_{\mathrm{air}} \sim 1.22\ \mathrm{kg\,m^{-3}}$ is the air density, U is the wind speed and C_D the drag coefficient. C_D is a non-linear function of the wind speed and was computed as [Large and Pond, 1980]:

$$\mathrm{C}_D = \begin{cases} 2.18 \times 10^{-3} & \text{for } U \leq 1\ \mathrm{ms^{-1}} \\ (0.62 + 1.56 \cdot \mathrm{U}) \times 10^{-3} & \text{for } 1\ \mathrm{ms^{-1}} < U < 3\ \mathrm{ms^{-1}} \\ 1.14 \times 10^{-3} & \text{for } 3\ \mathrm{ms^{-1}} \leq U \leq 10\ \mathrm{ms^{-1}} \\ (0.49 + 0.065 \cdot \mathrm{U}) \times 10^{-3} & \text{for } U > 10\ \mathrm{ms^{-1}} \end{cases} \tag{2.3}$$

The wind stress will be used to describe the vertical profile of the TKE dissipation, when it is induced solely by the mechanical action of the wind [Jurado et al., 2012]: $\varepsilon{*}_s = u{*}^3/(\kappa z)$, where

$\kappa = 0.4$ is the von Karman constant and $u_* = \sqrt{\tau/\rho}$ is the surface friction velocity. The correlation between $\varepsilon *_s$ and ε will be used to determine whether the vertical profile of ε follows the wall law in the WML [Anis and Moum, 1995].
Assuming salinity negligible, the buoyancy flux was determined as $B_0 = g\alpha Q_o/(\rho C_p)$ [Wuest and Lorke 2003], where g = 9.81 m s^{-2} is the acceleration of gravity, α is the coefficient of thermal expansion, ρ is the surface water density and C_p is the specific heat of the surface water. All the lake influx are considered positive in this analysis. In the turbulent kinetic energy budget, the buoyancy flux term quantifies the turbulent energy consumption as work against the stratification or the convective turbulent energy production. In the same way, the surface buoyancy flux B_o describes the stabilizing/destructive action of the surface heat flux on the stratification.
The Monin-Obukov length was computed as[5] $L_{MO} = u_*^3/(\kappa B_o)$, and it indicates the relative magnitude of wind generated turbulence against the stratification (regulated by the buoyancy flux B_o).

3 Results and discussion

3.1 Metereological Forcing

The wind pattern on Lake Garda is quite regular. The wind conditions found during the survey are shown in fig.3.1: a thermal wind blowing from South/South-West called Ora del Garda (which we will refer to as Ora) sets at midday until the sunset as a moderate breeze, 6.2 m/s on average; the Peler wind from North blows in the morning with an average intensity of 3.5 m/s; the Foehn, a warm and dry down-slope wind blowing on the lee-side of the mountains. Remarkable conditions were found on the 10 of March when the steady Foehn blew the whole day from North/North-East (with an average speed of 3.5 m/s), and on the 6th of April when we observed a moderate breeze (6.8 m/s) of Peler being followed by the Ora thermal wind with an average intensity of 9.2 m/s.

[5]Although, in literature, the equation for the Monin Obukov length is usually written as $L_{MO} = -u_*^3/(\kappa B_o)$, this formulation is consistent with the heat flux sign convention used.

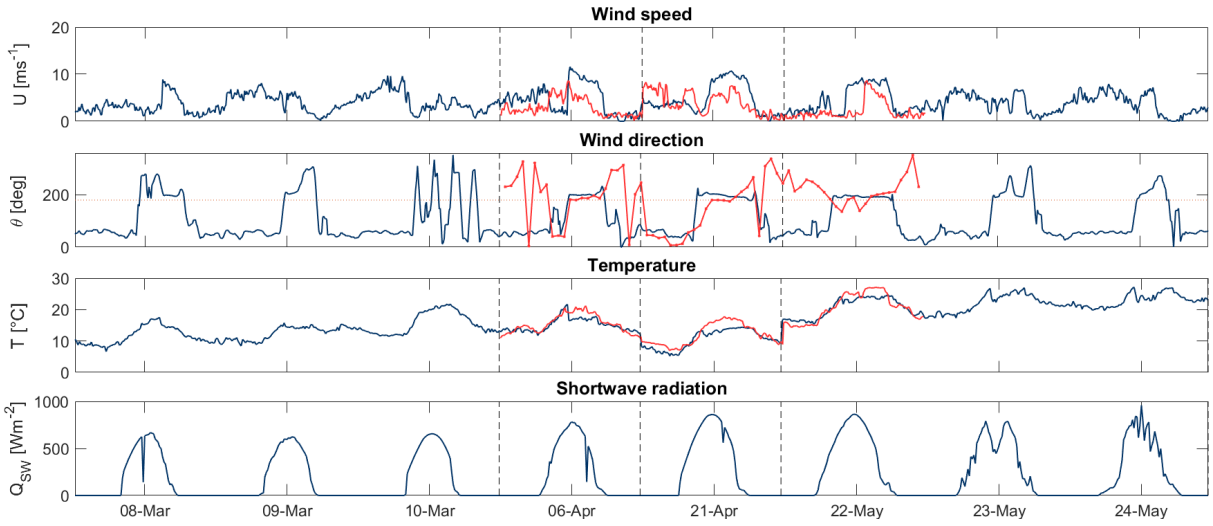

Figure 3.1: The atmospheric conditions measured in Torbole in blue and in Limone in red. The dashed lines separates discontinuous data.

Surface fluxes analysis The main sources of turbulence in the upper layer of a lake are: wind induced shear instabilities, wave breaking and sinking of denser water masses due to the surface cooling [Wuest and Lorke 2003]. During all the measuring campaign, no significant wave activity was encountered, thus it is reasonable to discard this process in the forcing analysis. In order to discriminate between the other two generation mechanisms, the surface heat fluxes and the surface wind stress were computed (as shown in section 2.3) and the results are presented in fig.3.2 along with the Monin Obukov length. During the survey, the total surface heat flux was always positive (towards the lake), hence we can also exclude turbulence production via convection.
The dominant component in the heat flux budget is the short wave radiation, hence the values of Q_o fluctuate around the mean $\overline{Q}_o$ = 568 W m^{-2} following the diurnal oscillation of the solar radiation. The top panel of fig.3.2 clearly exhibits this trend: in the morning the net surface heat flux increases until the peak is reached at noon; only on the 23rd and 24th of May, the net surface heat flux is weakened by the cloud coverage while, on all the other days, the cloud coverage was not significant. The buoyancy flux is always positive and consistent with the net surface heat flux, thus, it always acts to stabilize the surface layer. The relative strength of the wind induced turbulence against the buoyancy flux is described by the Monin Obukov length L_{MO}, plotted in the last panel of fig.3.2 (green dotted line) along with the WML depth (light blue line): for all the stations, the L_{MO} is positive showing that the wind induced turbulence is always weakened by the stratification; the WML depth is larger than L_{MO} in most of the stations and the average Monin Obukov length

is $\overline{L}_{MO} \sim 8.1$ m indicating that the mechanical action of the wind cannot explain the turbulent motion in the whole WML. On the 8th of March, the 6th and 21st of April, L_{MO} is larger than the WML depth, hence we expect the profiles of TKE dissipation to match those of $\varepsilon * _s$ and the wall law within the surface layer.

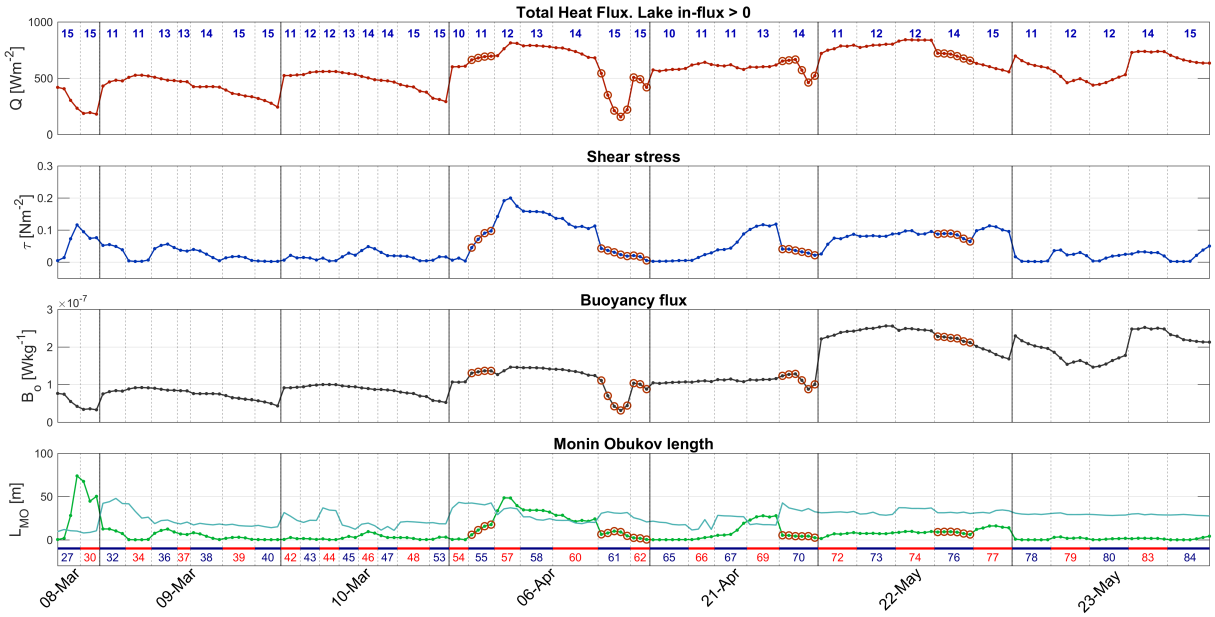

Figure 3.2: From top to bottom are plotted the time series of: Net Surface Heat Flux Q, Wind Shear Stress τ, Buoyancy Flux B_o, Monin Obukov length compared with the WML depth. On top of the first plot is written in blue the time of each station sampling, at the bottom of the last plot the id of the station is written in alternating red-blue colors. All the outputs were computed using Torbole meteostation data, with the exception of Limone's stations which are represented as circled red dots. In the fourth panel, the green dotted line represent the evolution of the Monin Obukov length while the smooth light blue line represent the well mixed layer depth.

Wind forcing of the Ekman circulation As anticipated, with the purpose of observing the Ekman circulation in Lake Garda, several longitudinal transects are here investigated. This type of flow is forced by the wind blowing along the lake's main axis, and it occurs as a closed circulation in the plane orthogonal to the wind direction. To determine if the proper wind conditions were met, in fig.3.3-right the time series of wind speed measured in Torbole is plotted for all the transect's profiles along with the type of wind (Peler, Ora, Foehn).

For the 10th of March two transects are available, so that we are able to compare the morning with the afternoon patterns (1st and 2nd rows of fig.3.7). On this day a weak Foehn wind from the North

prevailed over the Peler-Ora cycle, with an average intensity of 3 ms^{-1}.
Torbole's meteorological station measured on the 21st of April the typical Peler-Ora wind cycle, after 3 days of strong constant Foehn wind from NE (fig.3.3-left). Even if at the time of sampling the wind did not preserve its direction, the Foehn wind in the previous days was able to set an Ekman circulation, which would last until next day.

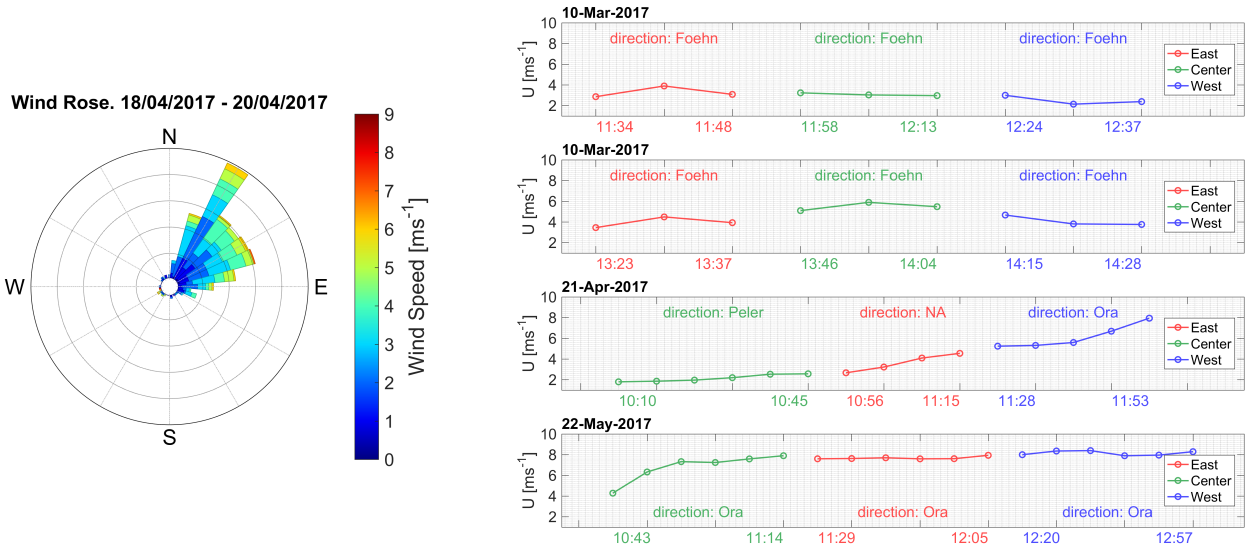

Figure 3.3: Left: Wind Rose representing the wind conditions before during the 3 days previous 21-Apr-2017. The radial axis represents the frequency of appearance (histogram), the angle express the wind origin. Right: Plots of the wind speed found during the Transect's survey. The lines represent the wind speed U in ms^{-1} measured in Torbole (the most representative station on the lake) against time, the dots correspond to the different profile within each station. The different colors discriminate between different location and the wind direction is stated for each station. On the x-axis the initial and final time of every surveyed station is written in colors matching the proper location.

3.2 Inter-seasonal variability of the surface layer

APPA is the main site of the survey. At this position, 122 profiles were studied during 8 different Spring days, with an average of 17 profiles per day. This large ensemble of data provides us the means for an investigation of diurnal variation and of the evolution of the WML in time during the Spring months.
In fig.3.5-mid, the depth binned temperature is plotted for the three different months. During the early Spring (until st. 60), the thermal vertical structure of Lake Garda presents an thick homogeneous WML in the morning, which in time, becomes thinner and more stable as a result

Table 3.1: Mean surface water temperatures in °C

Data	8-Mar	9-Mar	10-Mar	6-Apr	21-Apr	22-May	23-May
Climate	8.02	8.04	8.06	9.27	10.28	13.93	14.07
APPA	9.21	9.02	9.08	9.15	9.27	13.31	14.25
Limone	NA	NA	NA	9.78	9.48	13.67	NA

of the surface heating: an average variation $\Delta Z_{\mathrm{WML}} \sim 20$ m of the WML depth is observed. In late Spring a stable stratification is observed during the whole day with a WML that extends to $Z_{\mathrm{WML}} \sim 30$ m. In tab.3.1, the daily averaged surface temperature is compared with the climatic mean computed with the outputs of the air2water model [Piccolroaz, 2016]: during March, values well above the climatic mean are reported, on April instead the surface temperature is colder than the climatic mean. Particularly, stations 27 and 30, sampled on the 8th of March, exhibit a very warm surface layer, with an average temperature $\mathrm{T_{WML}} \sim 9.02$ °C and a surface temperature of T(z=0) ~ 9.21 °C: due to an unusual warm layer, the WML depth is observed at 10 m, the shallowest depth recorded. The vertical profiles of dissipation of TKE (fig.3.5-top) show larger values during the morning than in the afternoon, as a consequence of the weak morning stratification and the diurnal warming of the surface layer. The first five meters of depth are always the most dissipative, with ε ranging from a minimum $\varepsilon_{\mathrm{min}}\big|_{z\sim 1.75} \sim 5.17 \cdot 10^{-9} \mathrm{m^2 s^{-3}}$ (Station 065) to a maximum of $\varepsilon_{\mathrm{min}}\big|_{z\sim 1.75} \sim 2.02 \cdot 10^{-6} \mathrm{m^2 s^{-3}}$ (Station 060).

During March and April, significant values of TKE dissipation are also found outside the WML: for all these profiles (stations: 32, 34, 37, 43, 54, 65), the station averaged Monin Obukov length $< \mathrm{L_{MO}} >$ is less than the 30% of the station averaged WML depth, therefore the wind may induce the turbulent motion only right below the surface. A comparison between the scaled TKE dissipation rates of station 32 and station 57 is shown in fig.3.4: here the x-axis represents the TKE dissipation rate scaled with $\varepsilon {*_s}$[6], the y-axis represents the depth scaled with the WML depth. Station 57 was chosen due to the strong wind stress recorded during the measurements, station 32 was selected due to large values of ε found close to the WML depth.

In fig.3.4-left, the vertical profile of the scaled TKE dissipation rate is far from constant, implying that ε does not scale with $\varepsilon {*_s}$. The result for station 57 shows that ε scales with $\varepsilon {*_s}$, supporting the hypothesis that the turbulence within the WML is generated by the mechanical action of the wind at the surface. The scale factor computed as the station averaged ratio of ε and $\varepsilon {*_s}$ is $\sim 0.01 << 1$. The very low proportionality constant is attributed to the quality of the wind data, as the on-land

[6] $\varepsilon {*_s}$ computation was discussed in the Meteorological forcing section

meteorological stations cannot capture the in-situ fluctuations of the wind.

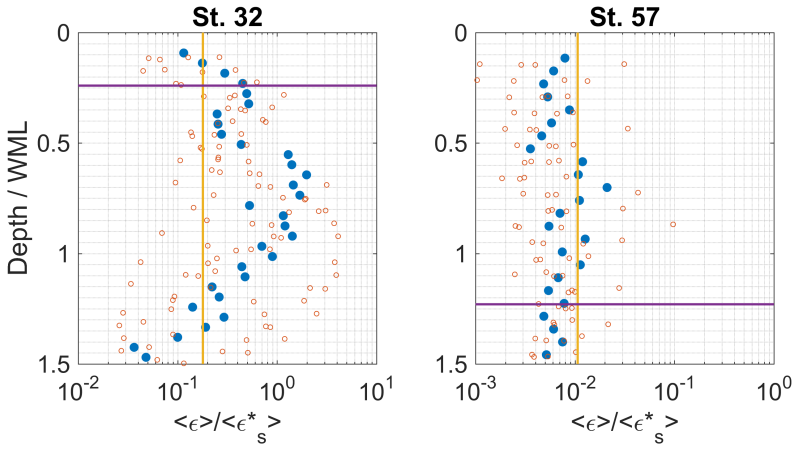

Figure 3.4: TKE dissipation rate scaled with $\varepsilon*_s$ plotted against the depth scaled with the WML depth. The red vertical line represent the scale factor computed as the station averaged ratio $\varepsilon/\varepsilon*_s$ within the WML depth; the horizontal purple line represents the ratio between the Monin Obukov length and the WML depth. The empty dots represent the scaled TKE dissipation rate for all profiles, the filled dots represent their station average.

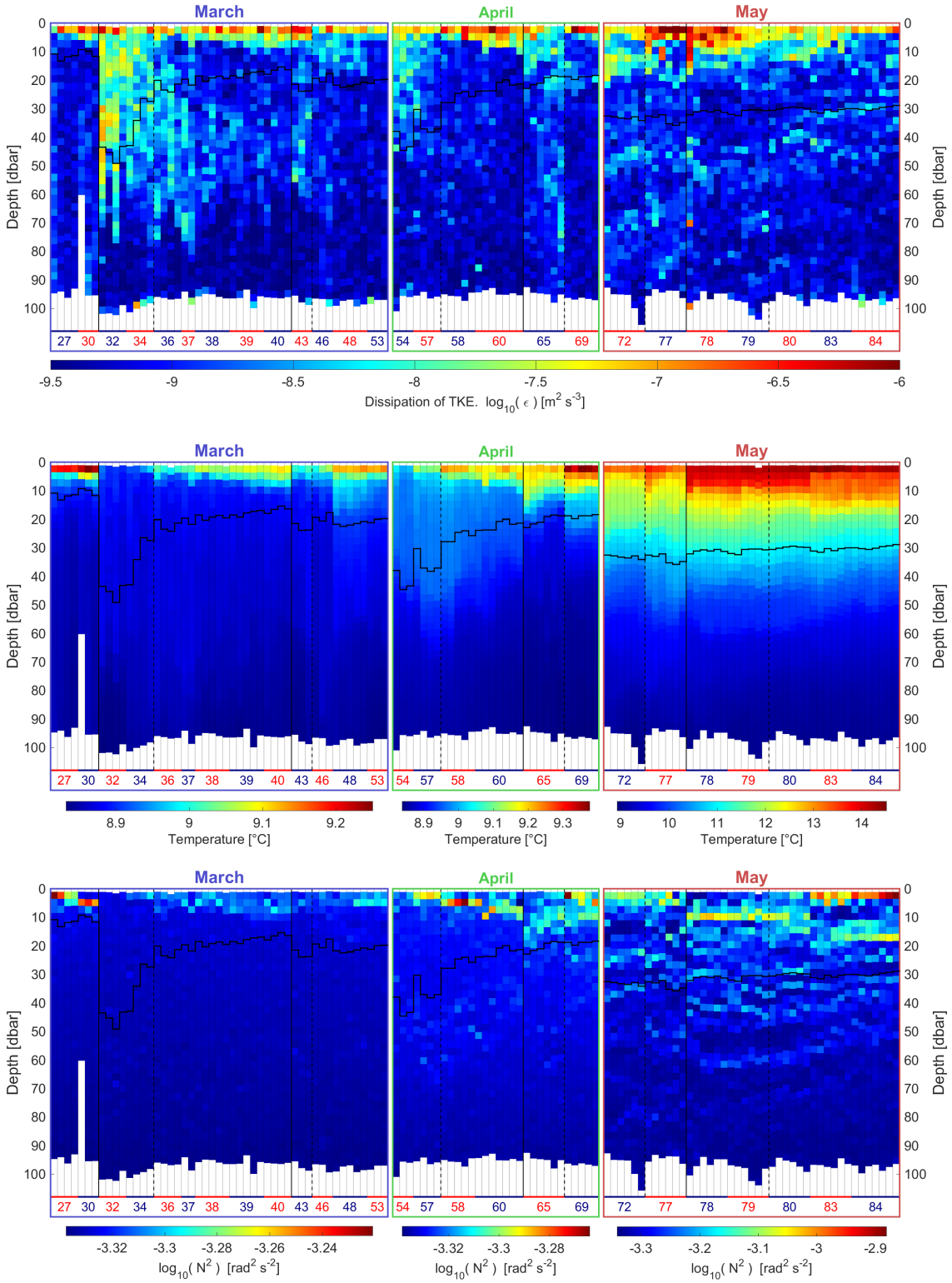

Figure 3.5: In all the plots: the horizontal red-blue line identify each station, the vertical solid black lines separate different days, the vertical dashed lines separate mornings from afternoons.The black step-wise constant line represent of the maximum depth of the WML. From top to bottom: the vertical depth binned profile of TKE dissipation rate ε; the vertical depth binned profile of temperature (Slow response thermistor JAC_T); the vertical depth binned profile of Brunt-Vaisala frequency squared N^2 (log scale)

3.3 Longitudinal variations and Ekman vertical transport

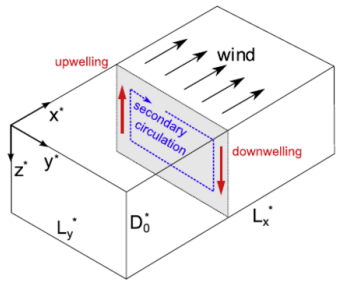

Figure 3.6: Sketch of the Ekman circulation in a simplified basin. Courtesy of M. Toffolon [2]

When the wind blows in the direction of the lake's main axis, a vertical flow is expected at the sides of the basin while horizontal advective transport should arise in the bottom and surface layers as depicted in fig.3.6. We will focus on the lake sides convective motion, based on the analysis of the vertical profiles of Temperature, Chlorophyll and vertical Diffusivity surveyed during March, April and May.

On the 10th of March the Ekman circulation was observed, and a proof is found in the temperature profiles in fig.3.7: here the plots of binned vertical temperature profiles are shown for each station, arranged in the East, Center and West order[7]. For all the profiles within the eastern station (left), the the surface temperature does not exceed 9 °C, either during the morning or the afternoon, and the water below the WML depth is completely homogeneous; on the western side instead, surface temperatures above 9.1 °C are observed. The WML is found at 40 m on the western boundary, across which lies a homogeneous layer of warm waters due to the Ekman downwelling (between the 15 m and the 50 m depths). Here the downward transport of surface water widen the vertical extent of the stratification, hence a deeper thermocline is observed. On the eastern side, the upwelling of colder water generates steeper gradients closer to the surface, resulting in the shallowing of the WML. In the afternoon, along with the warming of the surface layer, we observe the WML shallowing at all locations. The morning vertical diffusivity profiles present strong mixing processes at the surface, as a direct consequence of the wind induced turbulence. A clear evidence of the downwelling motion is found in the eastern station, where significant values of the mixing coefficient are detected across and below the thermocline (1st row 3rd column of fig.3.7). The vertical mixing in the West is mostly confined into the WML, thus it is directly influenced by the local atmospheric conditions. At the center of the transect the conditions remain constant during the day, therefore no evidence of the East-West advection is observed.

Fig.3.7-3rd row clearly illustrates a complete homogeneous cold water column at the eastern side (left) of the transect, with a mean surface temperature of 8.8 °C, much lower than the respective climatic values of 10.28 °C: this vertical thermal homogeneity is a direct consequence of the Ekman upwelling of deep cold water into the surface layer. The WML depth is not representative of the

[7] Hence not in the chronological order in which they were sampled

bottom boundary of the surface mixed layer, since the water column is completely mixed. The effects of the upwelling motion are also found in the mixing coefficient vertical profiles. Below the themocline very large values of K_T, compared to the rest of the transect, are found down to the 95 m of depth, suggesting that the column is completely mixed. In the west and in the center, the mixing is mainly wind-induced and confined to the surface layer.

The central and western points of the transect share a similar vertical thermal structure, being both the surface layers characterized by a strong stratification and shallowing thickness. The western surface layer is at the same time warmer and deeper than the central one: the WML depth lies on average at 27 m, 10 meters deeper than the central one, and its average[8] temperature is 0.1 °C warmer. On this basis we may conclude that a downwelling of surface waters happened in the western point of the transect.

Regarding the 22nd of May, we expected to observe a "reverse" Ekman circulation, with downwelling at the east and upwelling at the west the presence of a steady Ora wind (from South) . The temperature profiles of the transect do not present any significant asymmetry between the two sides of the lake, specifically no signs of upwelling water is found in the west. We may conclude that on this occasion, the atmospheric and lake's conditions were not suitable to set in motion the Ekman circulation. By comparing the 2 previous study cases (10-Mar and 21-Apr), the main substantial difference is the magnitude of the stratification. In May the higher air temperatures and stronger solar radiation result in the most intense and persistent surface buoyancy flux, setting a stratification able to suppresses the vertical transport at the sides of the transect.

[8]here the average is computed as the algebraic average of the mean temperature between the surface and the WML bottom boundary.

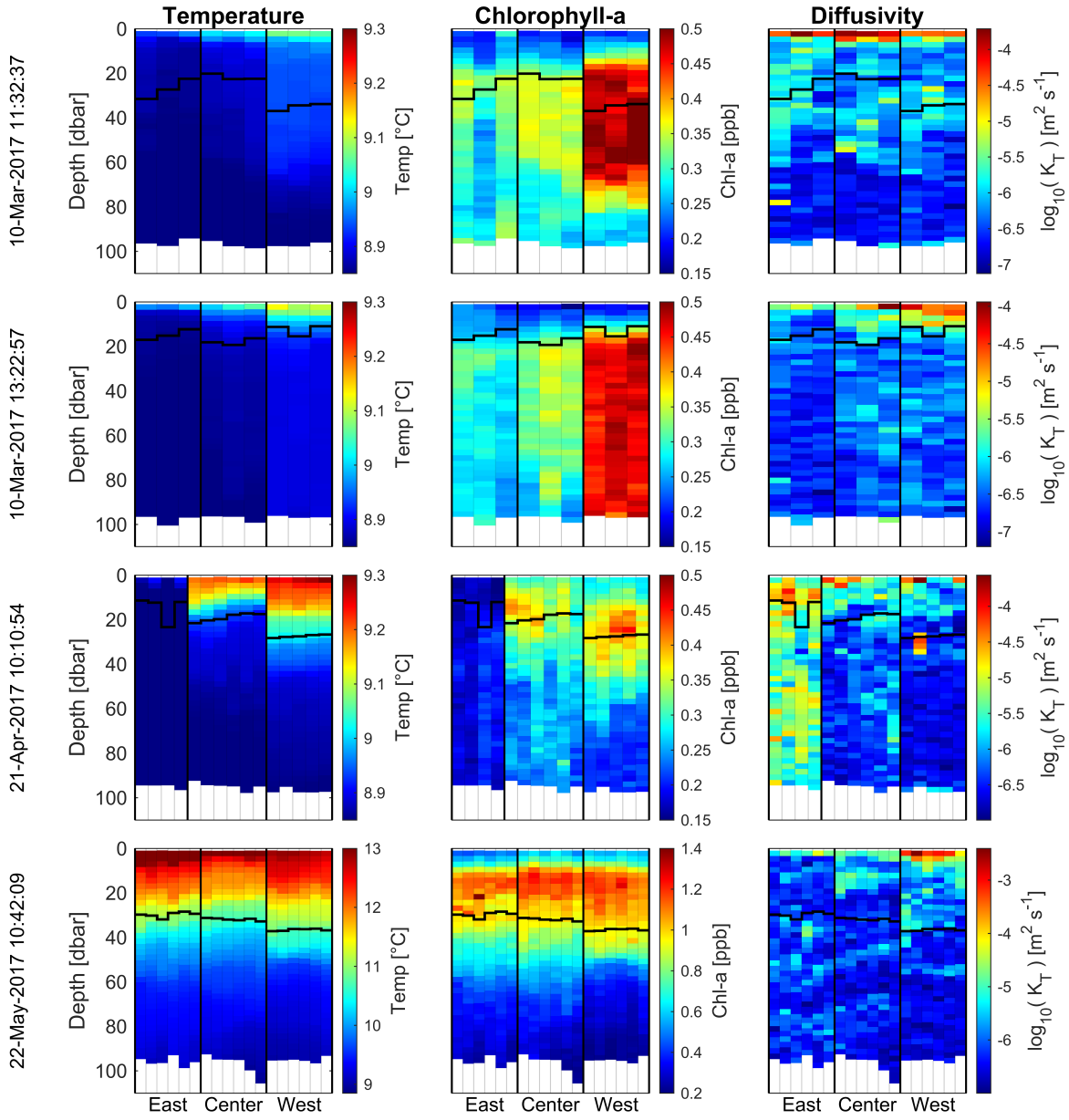

Figure 3.7: The plots above represent the evolution of temperature (left) and chlorophyll (right) profiles along the longitudinal transects. The date and time are specified in the title, each column of plots represent a location within the transect (west, center/APPA, east).

3.4 Spatial and diurnal variability of the surface layer

Vertical profiles of dissipation of TKE ε, temperature (sampled with the accurate slow thermistor "JAC T") and Brunt Vaisala frequency squared N^2 are here investigated for the months of April and

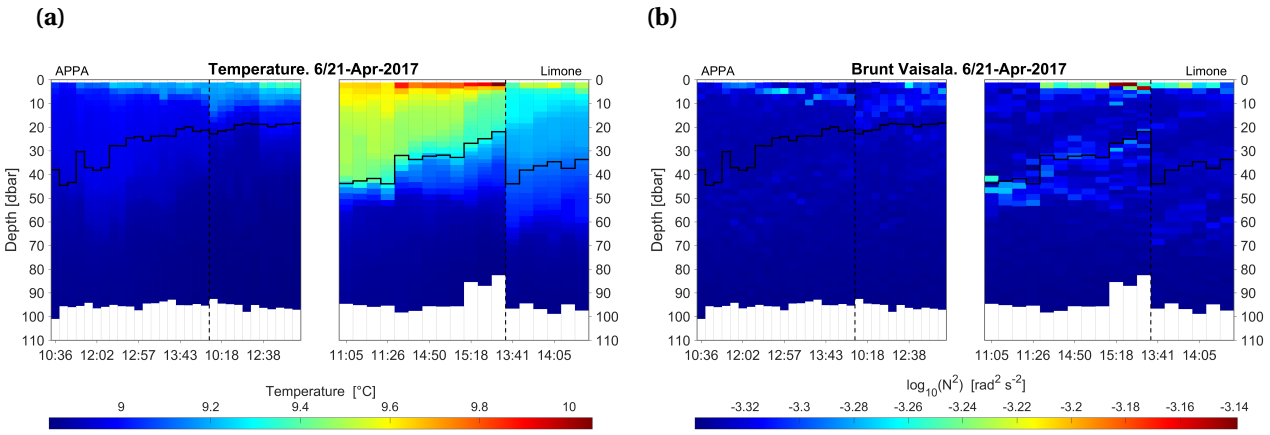

Figure 3.8: Comparison between APPA and Limone's vertical profiles of temperature (3.8a) and stratification (3.8a) measured in April. The vertical dashed black line separates different days (left the 6th, right the 21st), the black step line represent the Well Mixed Layer (WML) depth. APPA's and Limone's vertical profiles are plotted respectively on the left and on the right.

May[9] in Limone and at the APPA site.

A comparison of APPA and Limone's vertical profiles of binned temperature is shown in fig.3.8a for the month of April. On the 6th, the measured standard deviations of temperature within the WML in APPA and Limone are respectively 0.1 °C and 0.3 °C, and their mean are 9.15 °C and 9.78 °C: Limone presents a warmer surface layer than APPA's and a mean temperature half a degree higher than the climatic mean; the APPA water column is more homogeneous and its surface temperature is below the climatic mean. The maximum temperature of 10.05 °C (almost 1 degree above the climatic average, tab.3.1) is observed in Limone.

The WML depth is not clearly defined at the APPA site, since the surface layer is almost homogeneous (fig.3.8a-left): the Brunt Vaisala frequency shows very low variability and displays significant values only at noon, when the short wave radiation reaches its peak. Despite the momentum flux reaches the maximum value recorded (st. 57 in fig.3.2), the lake always appears stably stratified over layers of 2.5 m of bin. Due to the weak stratification, large values of dissipation of TKE are found mostly in the first 10 meters of depth: during the morning (until 11 am), the Peler wind blowing from North inhibits the stratification buildup, leading to dissipation of TKE even at 50 m depth (this feature was already analyzed in the APPA section 3.2). From 12:30 on instead, the Ora thermal wind sets from South at 8.5 m/s enhancing the turbulent motion and dissipation of TKE only at the surface.

[9]Limone was not surveyed in March

Limone's WML depth is well defined. Here strong temperature gradients are observed between 25 m and 50 m of depth, and the water column is stably stratified: as shown in fig.3.8b-right, the BV frequency presents larger values around the WML depth, with the only exception of the first 2.5 m during the afternoon. The well mixed layer becomes thinner and less homogeneous with time: according to fig.3.2 (st. 61 and 62), in the afternoon both the momentum and the buoyancy fluxes are weak, but the turbulent motion induced by the local wind (~ 5 ms^{-1}) is still suppressed by the stratification, hence the WML depth rises. Significant amounts of TKE dissipation rate are mostly observed during the morning (fig.3.10a)-left: the vertical profiles of ε range from $\varepsilon \sim 9.3 \times 10^{-8}$m^{2}s^{-3} at the surface to $\varepsilon \sim 9.3 \times 10^{-8}$m^{2}s^{-3} at the bottom boundary of the WML. In the afternoon, the turbulent dissipation at the surface is suppressed by the buoyancy flux, but it persists close to the thermocline, suggesting the presence of internal waves or seiches. The detection of internal wave motion was not achievable with the the CTD measurements.

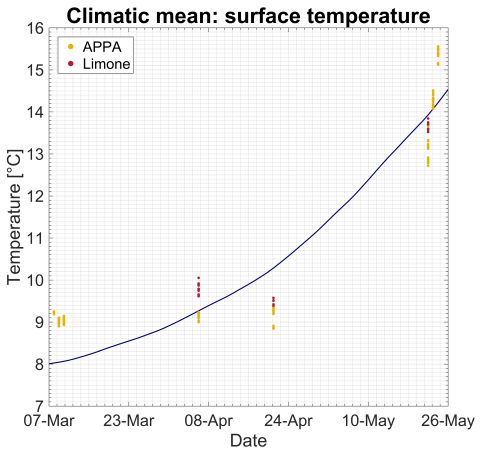

Figure 3.9: The climatic mean of surface temperature. The annual trend was compute using the Air2Water model [S. Piccolroaz 2016]. The dots represent the surface temperature measured in situ with the microCTD: in yellow the APPA site, in red Limone.

On the 21st of April, both the mean surface temperature of APPA and Limone are below the climatic mean: during the night a minimum temperature of 5.2 °C was reached and a strong Foehn was observed on the previous three days, as shown by the wind rose in fig.3.3-left. Due to the drop in air temperature during the night, APPA's profiles are weakly stratified. The WML depth is located at 20 m, and the average BV frequency in the WML is N$^2 \sim 4.8 \times 10^{-4}$ cmp^{2}s^{-2}. The vertical profiles of TKE dissipation rate in fig.3.10a display an homogeneous and turbulent WML during the morning $\varepsilon \sim 1.3 \times 10^{-8}$m^{2}s^{-3}. At noon, when the shortwave radiation reaches its peak and the Ora blows at 10 ms^{-1}, the extent of the wind turbulent motion is limited to the first 5 meters of depth with $\varepsilon \sim 1.7 \times 10^{-7}$m^{2}s^{-3}. In Limone, the water column develops from an almost homogeneous state to a more stable configuration, with the WML depth ranging from 45 m to 35 m below the surface. From fig.3.8, 3 distinct temperature gradients are appreciable at the average depths of $z_1 \sim 15$ m, $z_2 \sim 35$ m, $z_3 \sim 60$ m. The presence of multiple thermoclines is a typical feature of Limone's profiles: here, the local wind is weak and discontinuous and multiple stable layers may develop on top of one another. Consequently, the BV frequency is largest at the surface, but also significant along

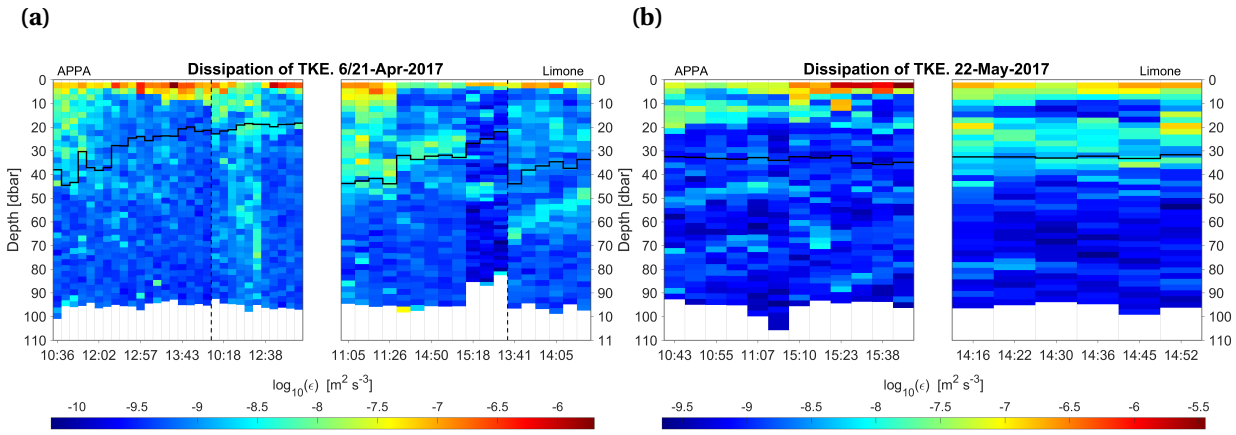

Figure 3.10: Comparison between APPA and Limone's vertical profiles of TKE dissiaption rate ε measured in April (3.10a) and in May (3.10b). The vertical solid black line separates different days (left the 6th, right the 21st), the dotted black line represent the well mixed layer depth (WMLD). APPA's and Limone's vertical profiles are plotted respectively on the left and on the right.

the three thermoclines. The wind forcing is mostly suppressed by the the buoyancy flux and, as a result of the strong stratification, induces the TKE dissipation mostly at the surface. Significant values of ε are found along the deepest thermocline $\varepsilon \sim 7.5 \times 10^{-9}$ m^{2}s^{-3}, which is too deep to be forced by the momentum flux at the surface. Instead, these deep patterns are most likely explained by internal waves motion.

On the 22nd of May the two sites present similar features, as the buoyancy flux dominates over the wind stress inducing a strong stratification in the WML. The mean surface temperature of APPA and Limone measures 13.31 °C and 13.67 °C respectively, both below the climatic mean ~13.93 °C. The WML is stably stratified: the observed temperature standard deviations within the WML are 0.65 °C in APPA and 1.5 °C in Limone, both are larger than April's variations by a factor of 5. The WML depth lies between 30-35 m below the surface and its depth remains constant in time.

In Limone two thermoclines are identified at $z_1^L \sim 15$ m, $z_2^L \sim 35$ m, both constant in time. At depths matching the two sharp temperature gradients, the BV frequency squared ranges from $N^2 \sim 5.26 \times 10^{-4}$ rad^{2}s^{-2} to $N^2 \sim 8.9 \times 10^{-4}$ rad^2 s^{-2}, thus dividing the WML into two parts. Furthermore, the largest values of the BV frequency are found at the deepest thermocline. In the upper WML, where the turbulence is directly forced by the wind, the TKE dissipation rate decreases from its maximum surface value[10] of $\varepsilon \sim 1.55 \times 10^{-7}$ m^{2}s^3 to $\varepsilon \sim 1.60 \times 10^{-9}$ m^{2}s^3 at the first thermocline. In the deeper WML, a thick turbulent layer is identified, where ε is almost uniform $\varepsilon \sim 1.6 \times 10^{-8}$ m^{2}s^3

[10]Computed as the station average of the first bin

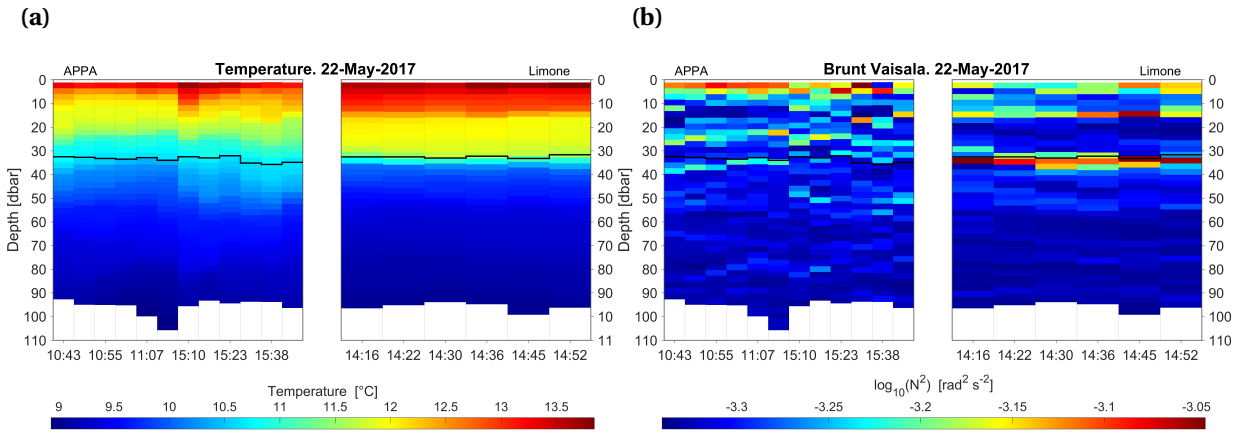

Figure 3.11: Comparison between APPA and Limone's vertical profiles of temperature (3.11a) and stratification (3.11a) measured in May. The black step line represent the Well Mixed Layer (WML) depth. APPA's and Limone's vertical profiles are plotted respectively on the left and on the right.

and largest at the first thermocline.

Also in APPA two thermoclines are observed (fig.3.11a-left) at $z_1^A \sim 25$ m and $z_2^A \sim 35$ m, resulting in the separation of the WML into two distinct sub-layers. In the afternoon, the shallow thermocline is not well defined: according to fig.3.2 st. 77, the buoyancy flux is minimum, while the momentum flux is enhanced, thus weakening the temperature gradients. In correspondence to the thermoclines (fig.3.11b-left), the BV frequency is strengthen and largest at the surface $N^2 \sim 4.8 \times 10^{-4} \text{rad}^2\text{s}^2$, unlike Limone's profiles where N^2 is largest at the deepest thermocline. As shown in fig.3.10b-left, the turbulent motion is mostly bounded between the surface and the shallow thermocline depth. The magnitude of ε at the surface increases in time as a consequence of the rising Ora, reaching its peak of $\varepsilon \sim 9.0 \times 10^{-4}$ m^2s^{-3}, which is the absolute maximum of ε recorded during the field work.

3.5 Phytoplankton and Mixing

Inter-seasonal variability The vertical binned profiles of Chl *a* concentration and the vertical binned profiles of thermal eddy diffusivity K_T, measured at the APPA site, are plotted in fig.3.13 for the months of March, April and May. For the months of March and April, the vertical variations of K_T are strongly dependent on the wind forcing, as the water column is stable but weakly stratified. The vertical profiles of the turbulent mixing coefficient, in fig.3.13-top, show a high mixing activity right below the air-water interface, where also the dissipation of TKE is the largest. At the wind dominated stations, large values of K_T, ranging from $K_T \sim 3\times10^{-6}\mathrm{m}^2\mathrm{s}^1$ to $K_T \sim 3\times10^{-5}\mathrm{m}^2\mathrm{s}^1$, are found at the middle of the WML; the mixing activity decreases towards the thermocline, below which turbulence is suppressed by the stronger stratification (st. 46-48-57-65). Remarkable vertical profiles were observed at stations 32 to 37 on the 9th of March: a steady moderate breeze from North is observed from 00:50 to 11:50, the turbulent mixing is maximum at the thermocline and it extends outside the WML. The deep mixing activity is observed also in the following profiles, it persists until 14:00 (~ 4 hr of sampling) and it shares the typical features of the Ekman downwelling profiles, studied in section 3.3. During May, the turbulent mixing is mostly bounded to the upper WML and the largest values of K_T are found at station 77, when the wind stress was strongest, and at station 78, when the cloud coverage significantly weakened the buoyancy flux and its stabilizing action.

In order to appreciate the distribution of the modest concentration of Chl *a* typical of March and April, different color scales are adopted. The peak of Chl *a* signal reached during the months of March and April is Chl *a*~ 0.5 ppb, which is smaller than half of the May's maximum Chl *a*~ 1.3 ppb. In the early Spring (stations from 27 to 60), the distribution of Chl *a* does not follow any definite trend, but it is rather dependent on the turbulent mixing that occurs in the morning. On the 9th March and 6th of April, because of the combined effects of the weak stratification and the strong wind forcing, the phytoplankton was able to sink deeper into the water column: in the morning, the Chl *a* is denser at the thermocline and it descreases toward the surface and outside of the euphotic zone; the following afternoon profiles show a much weaker concentration of Chl *a* trapped outside the WML. In the late Spring, we observe the phyoplankton bloom. The Chlorophyll vertical distribution is dominated by the stratification, which traps the Chl *a* in the WML. Coinciding with the local peaks of the wind stress, modest amounts of Chlorophyll are detected below the thermocline. Over the whole survey we oberve that almost no Chlorophyll is found in the first 10 m of depth, as the strong turbulent mixing dilutes the already modest concentration of Chl *a*.

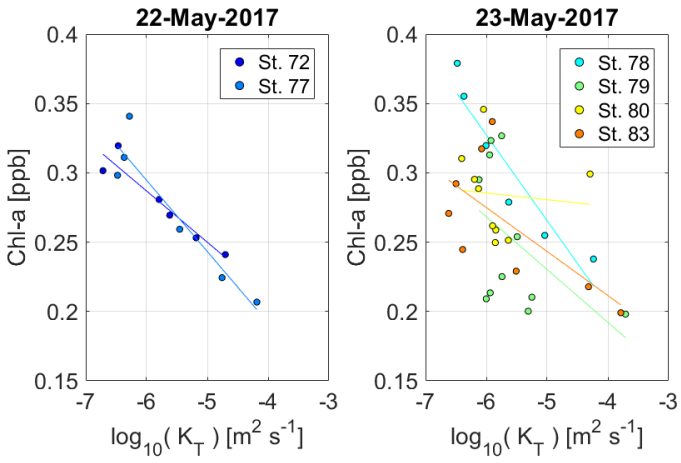

Figure 3.12: Correlation between Chl *a* and thermal eddy diffusivity K_T within the WML. The solind lines represent the Chl *a*-K_T linear regressions.

For the month of May the correlation between the Chl *a* and K_T in the WML was computed and plotted in fig.3.12: each dot identify for every binned depth the station average of Chl and K_T. All the station present a negative correlation between the two variables is found, the weaker correlation corresponds to station 80 where the turbulent mixing was weaker and extending at 10 m of depth. This supports the hypothesis of phytoplankton's turbulence avoidance [Pringle, 2007].

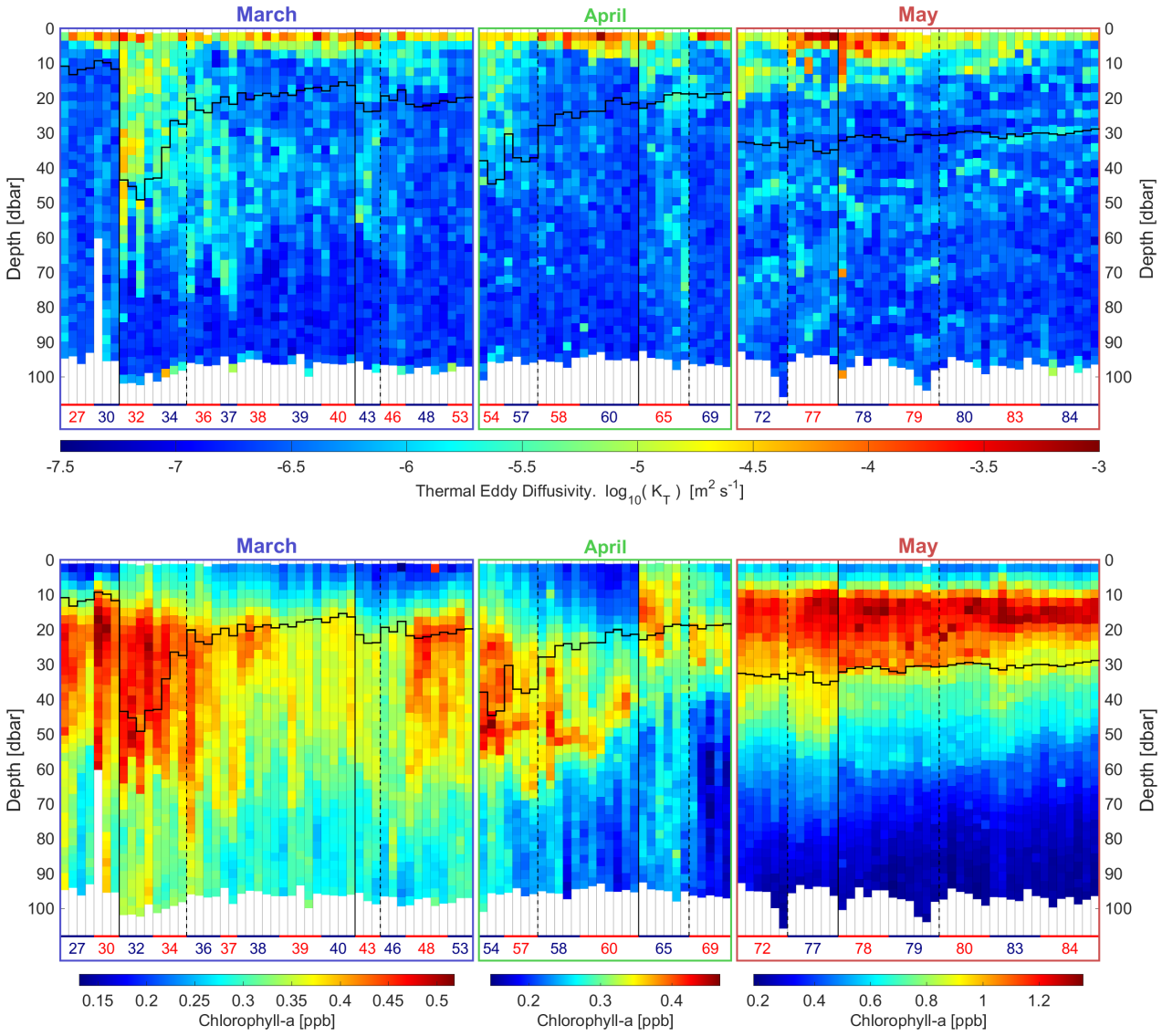

Figure 3.13: The top map represents the vertical depth binned profiles of thermal eddy diffusivity (log scale); the bottom map the vertical depth binned profiles of Chlorophyll *a*. The horizontal red-blue line identify each station, the vertical solid black lines separate different days, the vertical dashed lines separate mornings from afternoons. The black step-wise constant line represent of the maximum depth of the WML.

Spatial variability of Chlorophyll and turbulent mixing In April In Limone (fig.3.14-right) the high concentration of Chlorophyll-*a*, ranging from 0.55 to 1.1 ppb, is trapped beneath the 10 m and above the WML depth: the Chl *a* signal is most intense at 15 m below the surface, it decreases with depth (out of the reach of the solar radiation) and toward the surface, suggesting that phyto-

plankton activity may be inhibited by turbulent motion and direct solar radiation. On the other hand, at the APPA site, almost no chlorophyll was detected. Fig.3.14-right shows how the pattern of chlorophyll are strongly dependent on the lake stratification: in Limone from 11:26 on, the thermocline rises together with chlorophyll's maximum gradient, producing a convective motion of 25 m in 4.5 hours.

Fig.3.15-right clearly shows the phytoplankton blooming in APPA and in Limone for the month of May: in both cases the chlorophyll concentration is maximum at 20 m and decreases towards the surface and the thermocline, and its peak is detected in the afternoon. In Limone, the vertical distribution of chlorophyll remain constant in time. The strong stratification prevents the Chlorophyll from sinking in deeper waters, resulting in a sharp gradient of chlorophyll concentration at the bottom of the WML, where the concentration halves over 5 m. In APPA, a significant amount of Chlorophyll lies below the thermocline, with values ranging between 0.7 ppb and 0.9 ppb.

The turbulent diffusivity in APPA is more energetic during the afternoon and limited to the first 5 m of depth. The morning profiles in fig.3.15 show less intense mixing processes involving deeper waters. In Limone the conditions are completely different as 2 regions of mixing can be found: the first one is right below the surface and down to 5 m, this is the layer influenced directly by the wind; the second one is found at depths matching the one of the thermocline. These two layers are separated by relatively calm water. The turbulent mixing at the thermocline is typical of wind driven shear instability processes, which are the main sources of the turbulence during the measuring campaign (as also discussed in the Metereological forcing section 3.1), but could also

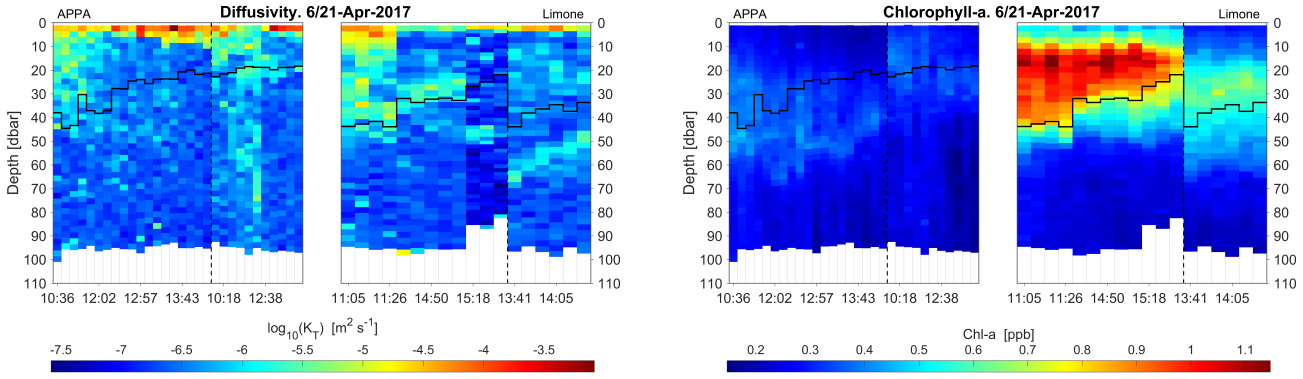

Figure 3.14: Comparison between APPA and Limone's vertical profiles of diffusivity (left) and chlorophyll-a (right) measured in April. The vertical solid black line separates different days (left the 6th, right the 21st), the dotted black line represent the well mixed layer depth (WMLD). APPA's and Limone's vertical profiles are plotted respectively on the left and on the right.

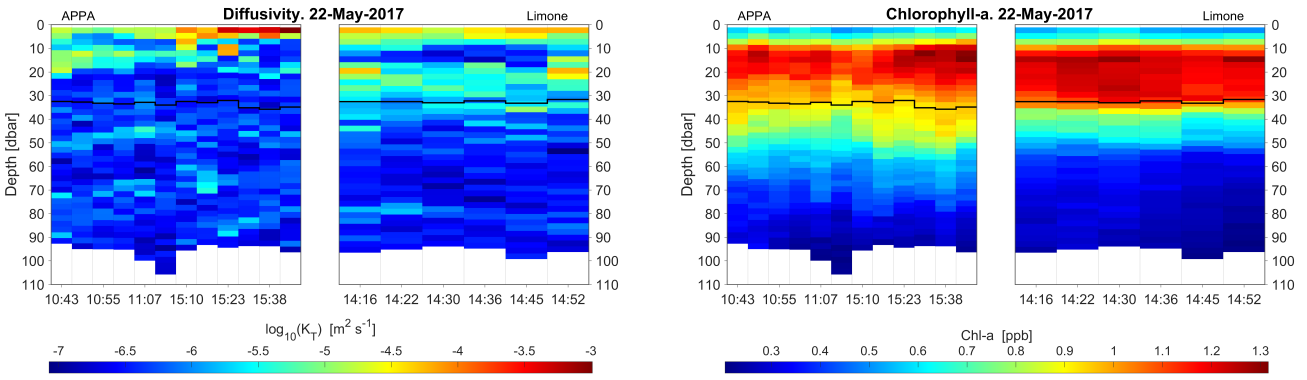

Figure 3.15: Comparison between APPA and Limone's vertical profiles of diffusivity (left) and chlorophyll-a (right) measured in May. The black step line represent the Well Mixed Layer (WML) depth. APPA's and Limone's vertical profiles are plotted respectively on the left and on the right.

be attributed to internal waves and seiches.

Effects of Ekman circulation on phytoplankton As previously discussed, the lateral boundaries of the longitudinal transects display a very different vertical structure than at the center of the lake, mostly caused by the wind induced Ekman circulation. We now investigate the phytoplankton population distribution and its development under these conditions, during the month of March and April. The amount of nutrients in the water column is the main factor affecting the growth of phytoplankton, hence the magnitude of the Chl *a* signal measured by the fluorimeter. The discrepancy between the total amount of Chl *a* measured in March and April is explained by the difference in strength of the deep turbulent diffusion of nutrients within the water column during the early Spring and and the late Spring: with more nutrients available in the water column, the growth rate of phytoplankton is higher. Fig.3.7-center shows how the Ekman transport substantially affects the Chl *a* horizontal distribution, with average concentrations growing from East to West. The lack of Chl *a* in the west is a direct consequence of the Ekman upwelling of bottom waters, rising from depths where the phytoplankton is unable to survive. A lack of Chl *a* is also found right below the water surface along all the transect, supporting the hypothesis that phytoplakton avoids highly turbulent waters: the negative correlation between K_T and Chl *a* is found in the well mixed layer (fig.3.16).In the central and western part of the lake the turbulent mixing is maximum at the surface and mostly bounded to the first 5 m of depth, which allows the growth of phytoplankton deeper in the water column: on the 10th of March, strong Chl *a* signal is found down to twice the depth of the thermocline during the morning and at the maximum sampling depth of the micro

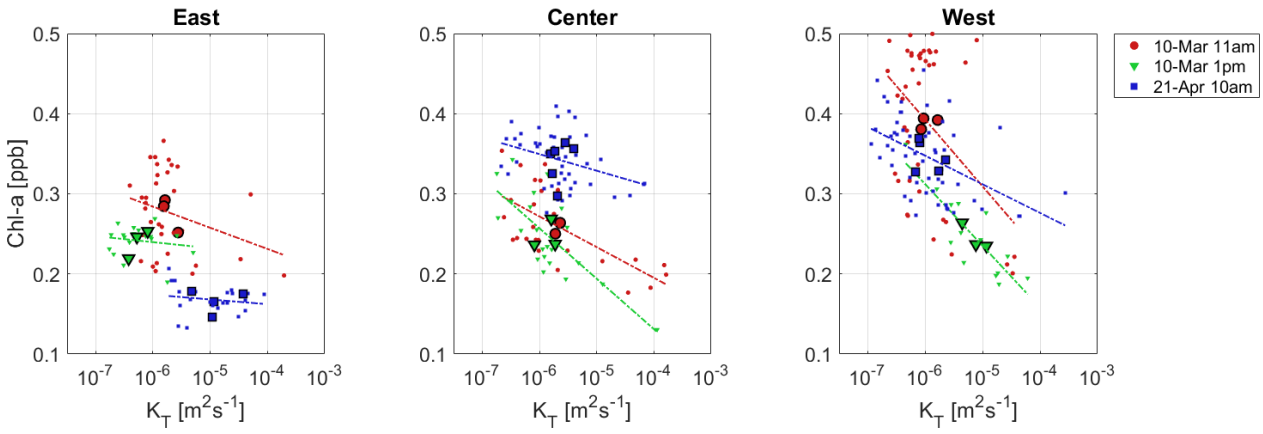

Figure 3.16: Correlation between Chl *a* and thermal eddy diffusivity K_T within the WML of each profile (Small dots). The station averages are identified by the larger markers. The dashed line represent the Chl *a*-K_T linear regression.

CTD (100 m) in the afternoon. The radiative forcing in April enhances the stratification, which in turn traps the Chlorophyll in the surface layer forming an unpper Chlorophyll maximum. Due to the Ekman-downwelling, however, part of the surface phytoplankton is able to sink below the thermocline. The deep Chl *a* progressively decreases towards the bottom as it leaves the euphotc zone (depths reached by the sun light and where the photosynthesis is possible). A deep chlorophyll maximum is clearly visible in the fig.3.7 in March plot: the strong chlorophyll signal, ranging from 4 to 5 ppb, extends from 20 to 80 meters, outside the typical euphotic zone. This unusual feature fits with the Ekman-downwelling observations: the downward transport transfers the surface phytoplankton through the euphotic zone (where it can photosynthesize) into deeper hostile conditions.

4 Summary and Conclusions

This study provided a description of the turbulent related-quantities and Chlorophyll distribution in the upper layer of Lake Garda. The analysis was based on the observations of the water vertical micro-structure, sampled during Spring 2017 using the microCTD.

Focusing on the inter-seasonal variability of the surface layer at the APPA site, we found the early Spring data to be highly dependent on the diurnal changes of the forcing, while a more stable vertical structure is induced by the buoyancy flux in the late Spring. Thus, the vertical profiles of ε presented a high vertical variability mostly at the beginning of the Survey. A negative correlation

between the Chl-*a* and K_T in the WML was found only in May, as the Chl-*a* concentration in March is much lower and diluted along the water column.

The parallel analysis of the TKE dissipation rate in APPA and Limone, along with the Ekman circulation analysis, exhibit the diversity of the turbulent processes in the Lake. The APPA site presented a strong mixing activity in the first 10 m of depth, being more exposed to the wind and less stratified. Limone is close to the shore and sheltered from the wind, thus its geographical features allowed the development of a stronger stratification: the dissipation rate of TKE below the air-water interface was on average weaker than in APPA, but deeper regions of dissipation were found along the sharp thermocline, a typical feature of internal wave induced turbulence.

The transects' data-set clearly showed the existence of strong convective motion at the side of the lake, attributed to the Ekman secondary circulation set by the wind and Earth's rotation. The observed vertical transport was maximum in March when the stratification was the weakest, with the wind blowing from the North: we found large amounts of Chl *a* sinking below the WML down to 90-100 m due to the downwelling in the West, and a water column completely depleted from the Chl-*a* by the up-welling in the East; it was found that the upwelling of cold water also induced strong turbulent mixing along the water column, while in the west the mixing processes are mostly bounded in the WML. During the May's transect sampling, the wind blew from South and a reverse circulation was expected, but due to the strong stratification, the vertical transport is almost completely suppressed. This results reflect the great impact of the secondary Ekman circulation on the phytoplankton life: the upwelling, along with the turbulent mixing, forces the depletion of phytoplankton in the East, while the downwelling forces the phytoplankton outside the euphotic zone, where it cannot photosynthesize.

A rough estimate of the anisotropy parameter (eq.1.1) gives $\alpha \sim 0.5 - 1.6$, considering: $D_0 \sim 250$ m computed as the mean depth of the transect, $W \sim 1500$ m the width of the transect, and $\nu_H/\nu_V \sim 10 - 100$. As we lack the observations of horizontal eddy viscosity, we based its estimation on the results from previous investigations of alpine lakes [Wang, 2002]. This estimate identifies lakes with moderate to strong anisotropy, where the lateral variation of vertical velocity is smooth, and the depth at which the maximum vertical transport is observed lies at 90 m ca, which fits with the observation of large amounts of Chl-*a* found at 100 m of depth at the western point of the transect on the 10th of March. In order to deepen the analysis of the secondary Ekman circulation, the estimation of the horizontal eddy viscosity and vertical transport are necessary, for instance using ADCP observations.

The large values of mixing coefficient in the first 5 m below the water surface are not consistent with the results from previous investigations of the WML of Lake Garda [Lenstra et al., 2014] and

in the Atlantic ocean [Jurado et al., 2012]. In these two studies, the turbulent related quantities were estimated from the measurements of the temperature microstructure by fitting the Batchelor empirical spectrum to the temperature gradient fluctuation spectrum [Oakey, 1982]. As shown in the methods section 2.3, here K_T was derived from the TKE dissipation rate and the Brunt Vaisala frequency, thus, when the stratification is weak, the vertical profiles of K_T resemble those of ε, explaining the large values of mixing coefficient at the surface. For further studies, the quality of the thermal eddy diffusivity estimation must be improved, either by a deep investigation of the mixing efficiency parameter for Lake Garda [Ruddick et Al., 1997], or by the implementation of a temperature microstructure based method.

A Appendix

A.1 RANS equation and Osborn turbulence model

Our starting point are the Navier-Stokes equations:

$$\frac{\partial u_i}{\partial t} + u_j \frac{\partial u_i}{\partial x_j} = -\alpha \frac{\partial p}{\partial x_i} - \delta_{i3} g - 2\varepsilon_{ijk}\Omega_j u_k + \nu \frac{\partial^2 u_i}{\partial x_j \partial x_j} \tag{A.1}$$

Where i = 1,2 are the two horizontal spatial direction and i=3 the vertical direction; u is the velocity vector, p the pressure, α the specific volume, g the acceleration of gravity, Ω the rotation vector, ν the kinematic viscosity, δ is the Kronecker delta and ε_{ijk} the permutation tensor. Repeated indices imply summation.

As turbulent flows are characterized by random 3D motion, a statistical analysis is necessary. In the next step, we will study the TKE variations using the Reynolds decomposition: we consider each variable (say ϕ) as the sum of its mean ($\overline{\phi}$) and its fluctuation (ϕ'):

$$u_i = \overline{u}_i + u_i' \tag{A.2a}$$

$$p = \overline{p} + p' \tag{A.2b}$$

$$\alpha = \overline{\alpha} + \alpha' \tag{A.2c}$$

For N and T large enough, we may assume the fluctuations to average to 0, thus if E[ ] represent

the averaging operator:

$$E[\phi] = E[\overline{\phi}] + E[\phi'] = \overline{\phi} \tag{A.3a}$$

$$\textbf{Time average: } E[\phi](s) = \frac{1}{T}\int_0^T \phi(s,t)\,dt = \overline{\phi}(s) \tag{A.3b}$$

$$\textbf{Ensamble average: } E[\phi](s,t) = \frac{1}{N}\sum_{k=1}^{N} \phi_k(s,t) = \overline{\phi}(s,t) \tag{A.3c}$$

Substituting the values in eqs.A.2 in eq.A.1 we obtain:

$$\frac{\partial}{\partial t}(\overline{u}_i + u'_i) + (\overline{u}_j + u'_j)\frac{\partial}{\partial x_j}(\overline{u}_i + u'_i) = -(\overline{\alpha} + \alpha')\frac{\partial}{\partial x_i}(\overline{p} + p') - \delta_{i3}g - \varepsilon_{ijk}\Omega_j(\overline{u_k} + u'_k) + \nu\frac{\partial^2(\overline{u}_i + u'_i)}{\partial x_j \partial x_j} \tag{A.4}$$

Multiplying by u'_i and averaging (according to eqs.A.3) the Reynold's averaged Navier-Stokes equation (RANS):

$$\begin{aligned} &u'_i\frac{\partial \overline{u}_i}{\partial t} + u'_i\frac{\partial u'_i}{\partial t} + u'_i(\overline{u}_j + u'_j)\frac{\partial}{\partial x_j}(\overline{u}_i + u'_i) = -u'_i(\overline{\alpha} + \alpha')\frac{\partial}{\partial x_i}(\overline{p} + p') - \delta_{i3}g + u'_i\nu\frac{\partial^2(\overline{u}_i + u'_i)}{\partial x_j \partial x_j} \\ &\frac{1}{2}\frac{\partial \overline{u'_i \cdot u'_i}}{\partial t} + \frac{\overline{u}_j}{2}\frac{\partial \overline{u'_i \cdot u'_i}}{\partial x_j} = -\overline{u'_i \cdot \alpha'}\frac{\partial \overline{p}}{\partial x_i} - \overline{\overline{\alpha}u'_i \cdot \frac{\partial p'}{\partial x_i}} - \overline{u'_i \cdot \alpha' \cdot \frac{\partial p'}{\partial x_i}} + \nu\overline{u'_i\frac{\partial^2 u'_i}{\partial x_j \partial x_j}} - \overline{u'_i \cdot u'_j}\frac{\partial \overline{u}_i}{x_j} \end{aligned} \tag{A.5}$$

If we define the material derivative as the local derivative with respect to time plus the mean flow advection[11], and rearranging the terms in eq.A.5, we obtain the Turbulent Kinetic Energy (TKE) balance:

$$\begin{aligned} &\frac{\mathrm{D}\,(\mathrm{TKE})}{\mathrm{d}t} = -\overline{u'_i \cdot \alpha'}\frac{\partial \overline{p}}{\partial x_i} - \overline{u'_i \cdot (\overline{\alpha} + \alpha') \cdot \frac{\partial p'}{\partial x_i}} + \nu\frac{\partial}{\partial x_j}\overline{(u'_i \cdot \sigma'_{ij})} - \varepsilon - \overline{u'_i \cdot u'_j}\frac{\partial \overline{u}_i}{\partial x_j} \\ &\mathrm{TKE} = \frac{1}{2}(\overline{u'_i \cdot u'_i}) \qquad \textbf{Turblent Kinetic Energy} \\ &\sigma'_{ij} = \left(\frac{\partial u'_i}{\partial x_j} + \frac{\partial u'_j}{\partial x_i}\right) \qquad \textbf{Fluactating Rate of Strain} \end{aligned} \tag{A.6}$$

Eq.A.6 states that the Turbulent kinetic energy varies due to the:

- Work done by the buoyancy flux:

$$-\overline{u'_i \cdot \alpha'}\frac{\partial \overline{p}}{\partial x_i} \simeq \frac{g}{\overline{\rho}}\overline{u'_3 \rho'}$$

[11] $\frac{D}{dt} = \frac{\partial}{\partial t} + \overline{u}_i\frac{\partial}{\partial x}$

- Correlation among turbulent velocity, turbulent pressure gradient and specific volume:

$$\overline{-u_i' \cdot (\overline{\alpha} + \alpha') \cdot \frac{\partial p'}{\partial x_i}}$$

- Divergence of the viscous diffusion of TKE

$$\nu \frac{\partial}{\partial x_j} \overline{(u_i' \cdot \sigma_{ij}')}$$

- Dissipation of TKE:

$$\varepsilon = \nu \sigma_{ij}' \sigma_{ji}'$$

- Redistribution of TKE. This term consists in the product of the Reynold's stress times the mean shear:

$$-\overline{u_i' \cdot u_j'} \frac{\partial \overline{u}_i}{\partial x_j}$$

The ratio of the source term to the buoyancy flux is the flux Richardson number R_f. Scaling the equations and under the assumption of isotropic and homogeneous turbulence, the steady state turbulent energy budget reduces to:

$$\overline{u_i' \cdot u_j'} \frac{\partial \overline{u}_i}{\partial x_j} = -\varepsilon - \frac{g}{\overline{\rho}} \overline{u_3' \rho'}$$

Defining the thermal eddy diffusivity as:

$$K = g \frac{\overline{u_3' \rho'}}{\overline{\rho} N^2}$$

we can express K in terms of the flux Richardson number, the TKE dissipation rate and N^2:

$$K = \frac{R_f \varepsilon}{(1 - R_f) N^2} = \Gamma \frac{\varepsilon}{N^2}$$

Station	Casts	Date	Time	Comments	Latitude	Longitude
027	4	8-Mar-17	14:50	APPA	45° 50’ 47 ” N	010° 50’ 59 ” E
030	3	8-Mar-17	15:33	APPA	45° 50’ 51 ” N	010° 50’ 56 ” E
032	4	9-Mar-17	10:56	APPA	45° 50’ 36 ” N	010° 50’ 53 ” E
034	4	9-Mar-17	11:39	APPA	45° 50’ 29 ” N	010° 50’ 40 ” E
036	4	9-Mar-17	13:18	APPA	45° 50’ 36 ” N	010° 50’ 52 ” E
037	2	9-Mar-17	13:47	APPA	45° 50’ 50 ” N	010° 50’ 52 ” E
038	5	9-Mar-17	14:17	APPA	45° 50’ 37 ” N	010° 50’ 59 ” E
039	5	9-Mar-17	14:55	APPA	45° 50’ 50 ” N	010° 51’ 00 ” E
040	4	9-Mar-17	15:28	APPA	45° 50’ 60 ” N	010° 51’ 00 ” E
042	3	10-Mar-17	11:34	TRANSECT - East	45° 50’ 35 ” N	010° 51’ 16 ” E
043	3	10-Mar-17	11:58	TRANSECT - Center	45° 50’ 31 ” N	010° 50’ 54 ” E
044	3	10-Mar-17	12:24	TRANSECT - West	45° 50’ 43 ” N	010° 50’ 13 ” E
045	3	10-Mar-17	13:23	TRANSECT - East	45° 49’ 43 ” N	010° 51’ 08 ” E
046	3	10-Mar-17	13:46	TRANSECT - Center	45° 49’ 47 ” N	010° 50’ 41 ” E
047	3	10-Mar-17	14:15	TRANSECT - West	45° 50’ 02 ” N	010° 49’ 58 ” E
048	5	10-Mar-17	14:40	APPA	45° 50’ 35 ” N	010° 50’ 45 ” E
053	3	10-Mar-17	15:31	APPA	45° 50’ 37 ” N	010° 50’ 56 ” E
054	3	6-Apr-17	10:36	APPA	45° 50’ 34 ” N	010° 50’ 45 ” E
055	4	6-Apr-17	11:05	Limone	45° 49’ 01 ” N	010° 48’ 21 ” E
057	4	6-Apr-17	11:47	APPA	45° 50’ 26 ” N	010° 50’ 39 ” E
058	5	6-Apr-17	12:35	APPA	45° 50’ 22 ” N	010° 50’ 37 ” E
060	7	6-Apr-17	13:20	APPA	45° 50’ 42 ” N	010° 50’ 53 ” E
061	5	6-Apr-17	14:34	Limone	45° 49’ 01 ” N	010° 48’ 23 ” E
062	3	6-Apr-17	15:18	Limone	45° 49’ 04 ” N	010° 48’ 48 ” E
065	6	21-Apr-17	10:10	TRANSECT - Center	45° 50’ 38 ” N	010° 50’ 54 ” E
066	4	21-Apr-17	10:56	TRANSECT - East	45° 50’ 24 ” N	010° 51’ 16 ” E
067	5	21-Apr-17	11:28	TRANSECT - West	45° 50’ 40 ” N	010° 50’ 16 ” E
069	5	21-Apr-17	12:38	APPA	45° 50’ 47 ” N	010° 50’ 51 ” E
070	6	21-Apr-17	13:41	Limone	45° 49’ 00 ” N	010° 48’ 20 ” E
072	6	22-May-17	10:43	TRANSECT - Center	45° 50’ 38 ” N	010° 50’ 59 ” E
073	6	22-May-17	11:29	TRANSECT - East	45° 50’ 25 ” N	010° 51’ 23 ” E
074	6	22-May-17	12:20	TRANSECT - West	45° 50’ 47 ” N	010° 50’ 10 ” E
076	6	22-May-17	14:16	Limone	45° 49’ 06 ” N	010° 48’ 33 ” E
077	6	22-May-17	15:10	APPA	45° 50’ 45 ” N	010° 50’ 47 ” E
078	6	23-May-17	10:44	APPA	45° 50’ 30 ” N	010° 50’ 42 ” E
079	6	23-May-17	11:31	APPA	45° 50’ 10 ” N	010° 50’ 28 ” E
080	6	23-May-17	12:17	APPA	45° 50’ 17 ” N	010° 50’ 36 ” E
083	6	23-May-17	13:42	APPA	45° 50’ 43 ” N	010° 50’ 53 ” E
084	7	23-May-17	14:27	APPA	45° 50’ 45 ” N	010° 50’ 48 ” E
085	6	24-May-17	10:42	NIOZ Buoy	45° 42’ 51 ” N	010° 44’ 37 ” E
086	6	24-May-17	11:29	NIOZ Buoy	45° 42’ 54 ” N	010° 44’ 01 ” E
087	6	24-May-17	15:16	NIOZ Buoy	45° 42’ 40 ” N	010° 44’ 39 ” E

References

[1] N. Salmaso *"Effects of climatic fluctuations and vertical mixing on the interannual trophic variability of Lake Garda, Italy"*. Limnol. Oceanogr. 50(2), 2005, 553-565

[2] M. Toffolon *"Ekman circulation and downwelling in narrow lakes"*. Advances in Water Resources (2013) Volume 53, Pages 78-86.

[3] A. Kolmogorov *"Local structure of turbulence in an incompressible fluid at very high reynolds number"*. Doklady AN SSSR (1941) Volume 4, Pages 299-303.

[4] Uriel Frisch *"The legacy of A.N. Kolmogorov"*. Cambridge University press(1995).

[5] T. Osborn *"Estimates of the Local Rate of Vertical Diffusion from Dissipation Measurements"*. Journal of Physical Oceanography (1980) Volume 10, Pages 83-89

[6] N. Oakey *"Determination of the rate of dissipation of turbulent kinetic energy from simultaneous temperature and velocity shear microstructure measurements"*. Journal of Physical Oceanography (1982) Volume 12, Pages 256-271.

[7] J. Austin, J. Allen, *"Sensitivity of summer Lake Superior thermal structure to meteorological forcing"*. Limnology and Oceanography (2011) Volume 56, Pages 1141-1154

[8] C. Abdulla et al., *"Estimation of Mixed Layer Depth in the Gulf of Aden: A New Approach"*. PLoS ONE (2016).

[9] R. Woolway et al., *"Automated calculation of surface energy fluxes with high-frequency lake buoy data."* Environmental Modelling & Software (2015) Volume 70: 191-198.

[10] W. Large, and S. Pond. *"Open ocean momentum flux measurements in moderate to strong winds."* Journal of physical oceanography (1981) Volume 11: 324-336.

[11] E. Jurado, et al., *"Microstructure measurements along a quasiâĂŘmeridional transect in the northeastern Atlantic Ocean."* Journal of Geophysical Research: Oceans (2012), Volume 117.

[12] Anis, and J. Moum. *"Surface Wave-Turbulence Interactions. Scaling Îţ (z) near the Sea Surface."* Journal of Physical Oceanography (1995) Volume 25: 2025-2045.

[13] A. Wuest, A. Lorke. *"Small-scale hydrodynamics in lakes."* Annual Review of fluid mechanics (2003) Volume 35: 373-412.

[14] S. Piccolroaz *"Prediction of lake surface temperature using the air2water model: guidelines, challenges, and future perspectives"*. Advances in Oceanography and Limnology (2016) Volume 7: 36-50.

[15] J. Imberger *"Flux Paths in a Stratified Lake: A Review"*. Physical Processes in Lakes and Oceans. Coastal and Estuarine Studies (2013) Volume 54: 1-18

[16] J. Pringle, *Turbulence avoidance and the wind-driven transport of plankton in the surface Ekman layer*, Cont. Shelf Res (2007) Volume 27: 670-678.

[17] Y. Wang, *"Importance of subgrid-scale parameterization in numerical simulations of lake circulation"*. Advances in Water Resources (2002) Volume 26: 277-294.

[18] A. Wuest, A. Lorke *"Small-Scale Hydrodynamics in Lakes"*. Annual Reviews of Fluid Mechanics (2003) Volume 35: 373-412.

[19] W. Lenstra et al., *"Diurnal variation of turbulence characteristics in Lake Garda"*. Advances in Oceanography and Limnology (2014) Volume 5: 184-203

[20] B. Ruddick et al., "Variations in apparent mixing efficiency in the North Atlantic Central Water." Journal of Physical Oceanography (1997) 27: 2589-2605.